APPLIED SCIENCES AND ENGINEERING

Perovskite retinomorphic image sensor for embodied intelligent vision

Zhilong He[1]†, Hongxiao Duan[1]†, Jianmin Zeng[1,2]†, Jie Zhou[3]†, Xiaolong Zhong[1], Zhixin Wu[1], Shenzhou Ni[2], Ze Jiang[2], Guangjun Xie[2], Jung-Yong Lee[4], Yi Lu[5], Yonghong Zeng[5], Biao Zhang[5], Wu Bin Ying[4]*, Zhibin Yang[3]*, Zhang Zhang[2]*, Gang Liu[1]*

Retinomorphic systems that can see, recognize, and respond to real-time environmental information will extend the complexity and range of tasks that an exoskeleton robot can perform to better assist physically disabled people. However, the lack of ultrasensitive, reconfigurable, and large-scale integratable retinomorphic devices and advanced edge-processing algorithms makes it difficult to realize retinomorphic hardware. Here, we report the retinomorphic hardware prototype with a 4096-pixel perovskite image sensor array as core module to endow embodied intelligent vision functionalities. The retinomorphic sensor array, using a one photodetector–one transistor geometry to resemble retinal circuit with broadband, ultrahigh, and reconfigurable photoresponsivities, executes both adaptive imaging with a contrast enhancement of ~620% under a dim-lit intensity of 10 microwatts per square centimeter and an instantaneous one-dimensional feature extraction algorithm to decompose the origin visual scenarios into parsimoniously encoded spatiotemporal information. This retinomorphic system endows embodied intelligence with adaptive imaging, in situ processing, and decision-making capabilities and promises enormous potential for autonomous robot applications.

INTRODUCTION

Exoskeleton robots are human-centered systems that aim to revolutionize the way we assist people with disabilities to live their lives in close proximity to normal human beings (1, 2). Extension to handle more complicated daily tasks with improved assistance quality requires such robots to sense, recognize the environmental information, and make decisions intelligently. Among all biological senses in a nature world, visions are the most direct, efficient, and important methods for animals to interact with their surviving environments (3). For instance, the sensitivity of leaf tailed geckos' retina to light is 350 times better than that of human beings, which enables them to see colors at night (4, 5). Frogs have five classes of ganglion cells in their retina that decompose complex images into simple information of contrast, convexity, edge, darkness, etc. Facile recognition of these representative features can help geckos and frogs to catch preys and dodge predators agilely (6, 7). Using embodied intelligent vision to sense, recognize, and respond to real-time surrounding environments will surely empower exoskeleton robots to serve handicapped people better. In view of this, developing advanced retinomorphic computation devices and systems that simultaneously integrate ultrasensitive optical sensing, real-time retinal processing, and decision-making functions becomes increasingly critical for the next-generation exoskeleton robot applications.

An ideal embodied intelligent vision system should achieve accurate imaging of visual targets in light environments with various frequencies and intensities. In situ feature extraction is also indispensable to accelerate the visual target recognition and actuation by eliminating downstream transmission of redundant visual information to higher-order controller units (8). With these concerns, ultrasensitive and nonvolatily reconfigurable photoresponses are essential indices for the retinomorphic devices to achieve precise image sensing and synapse weight updating of the neural network algorithms, respectively (9). Unfortunately, although conventional Si-, Ge-, InGaAs-, and HgCdTe-based photodetecting devices have exhibited promising sensing capabilities in the broad visible to infrared spectrum (10–12), their intrinsic vulnerability of fixed photoresponsivity hinders direct application as core modules of hardware accelerators to perform instantaneous retinomorphic processing tasks. Because of the exotic carrier transport dynamics in atomically thin layers, two-dimensional (2D) van der Waals materials have been recently widely studied for retina-inspired sensor devices with reconfigurable photoresponses and simulated image encoding, enhancement, and target/motion recognition functions within small-scale (e.g., 8 by 8) retinomorphic sensor arrays (RSAs) (13–26). However, reduction in the vertical dimension of the material also attenuates the degree of light-matter interaction in the 2D nanosheets, which leads to small photoresponsivities (viz., <100 mA/W in a broadband spectrum) and weak dim-light sensing capability. Although high sensitivities can be realized via gate tuning in phototransistors (27, 28), a concurrent increase of the dark current and a decrease of the on/off ratio severely deteriorate the contrast and quality of acquired images. It is noteworthy that the lack of large-area synthesis and integrating capability of 2D materials also restricts hardware implementation of artificial retina that resembles the complete anatomic structure and functions of the biological visual systems. Instead of executing a specifically designed neural network algorithm on the sensor array, the state-of-the-art retinomorphic systems rely heavily on convolution to perform in situ feature extraction during the image sensing process. The convolution neural network (CNN), which is traditionally efficient in handling complex patterns, can only run its first layer operation via

[1]Department of Micro/Nano Electronics, School of Electronic Information and Electrical Engineering, Shanghai Jiao Tong University, Shanghai 200240, China. [2]School of Microelectronics, Hefei University of Technology, Hefei 230601, China. [3]School of Chemistry and Chemical Engineering, Shanghai Jiao Tong University, Shanghai 200240, China. [4]School of Electrical Engineering, Korea Advanced Institute of Science and Technology, Daejeon 34141, Korea. [5]Tianjin Jinhang Computing Technology Research Institute, Tianjin 300308, China.
*Corresponding author. Email: yingwubin@kaist.ac.kr (W.B.Y.); zhibinyang@sjtu.edu.cn (Z.Y.); zhangzhang@hfut.edu.cn (Z.Z.); gang.liu@sjtu.edu.cn (G.L.)
†These authors contributed equally to this work.

weighted multiplication and accumulation (MAC) in the optoelectric domain (*14–18*). The effectiveness of extracting sufficient features with convolution is therefore substantially limited for high-accuracy target recognition and judging tasks. In short, the realization of embodied intelligent vision hardware, lacking large-scale integratable, ultrasensitive, reconfigurable visual sensor devices and efficient edge-processing algorithms, remains challenging.

In this contribution, we report the full-hardware implementation of the retinomorphic system with a monolithically integrated 4096-pixel perovskite image sensor array as the core element to endow the embodied intelligent vision functionality. Beneficial from the strong broadband absorption, large photoresponse, controllable reconfigurability upon ion migration, and facile solution processability, organometallic halide perovskites can ensure large and tunable photoresponsivity and provide the large-area integrating capability that are considered compelling materials for the construction of retinomorphic hardware systems. Narrow bandgap (NBG) perovskite with strong ultraviolet–visible–near-infrared (UV-VIS-NIR) absorption, large on/off ratio, and reconfigurable photoresponsivity is used to fabricate a large-scale photodetector array on an amorphous Si thin-film transistor (a-Si TFT) panel. Because of the prominent modulation ability of the TFT driver, each one transistor–one photodetector (1T-1PD) pixel of the 4096-pixel RSA exhibits ultrasensitive and individual reconfigurable photoresponsivities that fulfill the dim-lit image sensing and synapse weight updating requirements of the retinal processing operations. An instantaneous one-dimensional feature extraction (ODFE) algorithm that can be fully projected on the RSA has been designed to solve the inefficient feature extraction problems arose by the widely adopted optoelectric domain convolution methodology. Upon feeding the effectively decomposed spatiotemporal information into a fully connected layer or a recurrent neural network premounted on the retinomorphic hardware, real-time visual target recognition and decision-making for exoskeleton robots' motion in complex lighting environments are demonstrated. This innovative retinomorphic computation system with instantaneous "see, recognize, and respond" capability promises enormous potential for future embodied intelligent vision applications.

RESULTS
Design of perovskite retinomorphic computation system
Natural creatures rely on a visual system to cope with the vast barrage of incoming light patterns (left of Fig. 1A), wherein the retina is sophisticated as an information-processing "accessible part of the brain" with marvelous anatomic complexity and functionality. In general, the retina consists of chemically and/or electrically interconnected neurons of photoreceptors (P), horizontal (H) cells, bipolar (B) cells, amacrine (A) cells, and ganglion (G) cells (*4*). They are arranged into an intricate network of three cellular layers and two modulating synaptic layers, not only functioning as a simple spatiotemporal prefilter for light adaption and sharpening but also serving as a neural computation circuit to convey an efficiently processed image to the downstream area of the brain. As depicted in the right of Fig. 1A, the photoreceptor senses incident lights with various wavelengths and intensities and converts them into physiological signals. The bipolar cells receive these signals and shunt them to the ganglion cells. The sensitivities of the photoreceptors and bipolar cells are intermediated by horizontal cells, guaranteeing high-fidelity image sensing in all lighting environments. Then, the excitory signals

are transmitted from bipolar cells to ganglions cells directly, while the inhibitions are delivered upon amacrine cell modulation. Last, feature-extracting computation is done in ganglion cells with either excitory or inhibitory signals, outputting compressed images for the next-level processing. Instead of reading a generic pixel representation of the original image, the downstream area of the brain receives a parsimoniously encoded set of features including sustained edge, moving edge, net convexity, net dimming, and darkness from the ganglion cells via visual nerves. Upon pooling the firings of feature-extracting ganglion cells in a weighted summation, the cerebral cortex recognizes the visual targets simply without any higher-level processing. It is this unique anatomic structure and function of the vision system that enable frogs to catch preys fast and precisely. Therefore, development of advanced retinomorphic computation system should be orchestrated by simplifying the intricate visual circuit into ternary parts of the sensing-perception assemblage (P, B, and G neurons), the photoresponse modulator (H and A neurons), and the brainoid cortex yet portraying their holistic visual function with advanced sensor devices.

With this concern, we use 1T-1PD cells based on perovskite photovoltaic devices to reproduce the above-described bigroup retina hierarchy (top left of Fig. 1B) and integrate them back-end-of-line monolithically into a 4096-pixel image sensor array for fully hardware implementation of the retinomorphic system. Because of the strong absorption in the UV-VIS-NIR spectrum, the very long charge recombination lifetime, the large photoresponsivity, and the on/off ratio, as well as the wide linear dynamic range (LDR), NBG organometallic halide perovskites have been widely studied for high-performance photovoltaic and photodetector applications (*29–31*). The intrinsic ion migration process occurred in perovskite (*32*), arising from the monovalent organic cations and halide anions with small activation energy and a modest coefficient of diffusion in solid-state thin films (*33–38*). When perovskite is subjected to external voltage bias or light illuminations, these mobile ions will migrate considerably. Such intrinsic ion migration phenomenon provides an exotic opportunity of nonvolatile photoresponsivity reconfiguration through modulation of the material's composition and the device energy band diagram (bottom left of Fig. 1B). Although unfavored for high-efficiency solar energy conversion applications, such switchable photovoltaic behavior offers a basic operating principle for synaptic weight updating in a retinomorphic computing paradigm. In combination with the sensitive photoresponse, reconfigurability and facile solution processability for large-area fabrication, perovskites are considered compelling materials for the construction of retinomorphic hardware systems. Here, NBG perovskite with the composition of $FA_{0.8}Cs_{0.2}Pb_{0.5}Sn_{0.5}I_3$ was designed to build an ultrasensitive and reconfigurable sensing-perception assembly of P, B, and G neurons with the device geometry of indium tin oxide (ITO)/poly(3,4-ethylenedioxythiophene):poly(styrene sulfonate) (PEDOT:PSS)/perovskite/C_{60}/bathocuproine (BCP)/Au (note S1 and figs. S1 to S3). MA-free and Cs-containing composition is used to enhance the photothermal stability of the material, while partial substitution of Pb with Sn lowers perovskite's toxicity for human-friendly usage. In particular, the inclusion of the Sn component and the Sn/Pb atomic ratio of 1 can minimize the bandgap of the material and extend its absorption coverage into short-wavelength NIR regions (*39*).

Underlying the perovskite photodetectors, a-Si TFTs function as both selectors to guarantee proper operation on target perovskite devices in the crossbar array via gate control and H/A modulators to regulate the photoresponses of the 1T-1PD retina pixels through
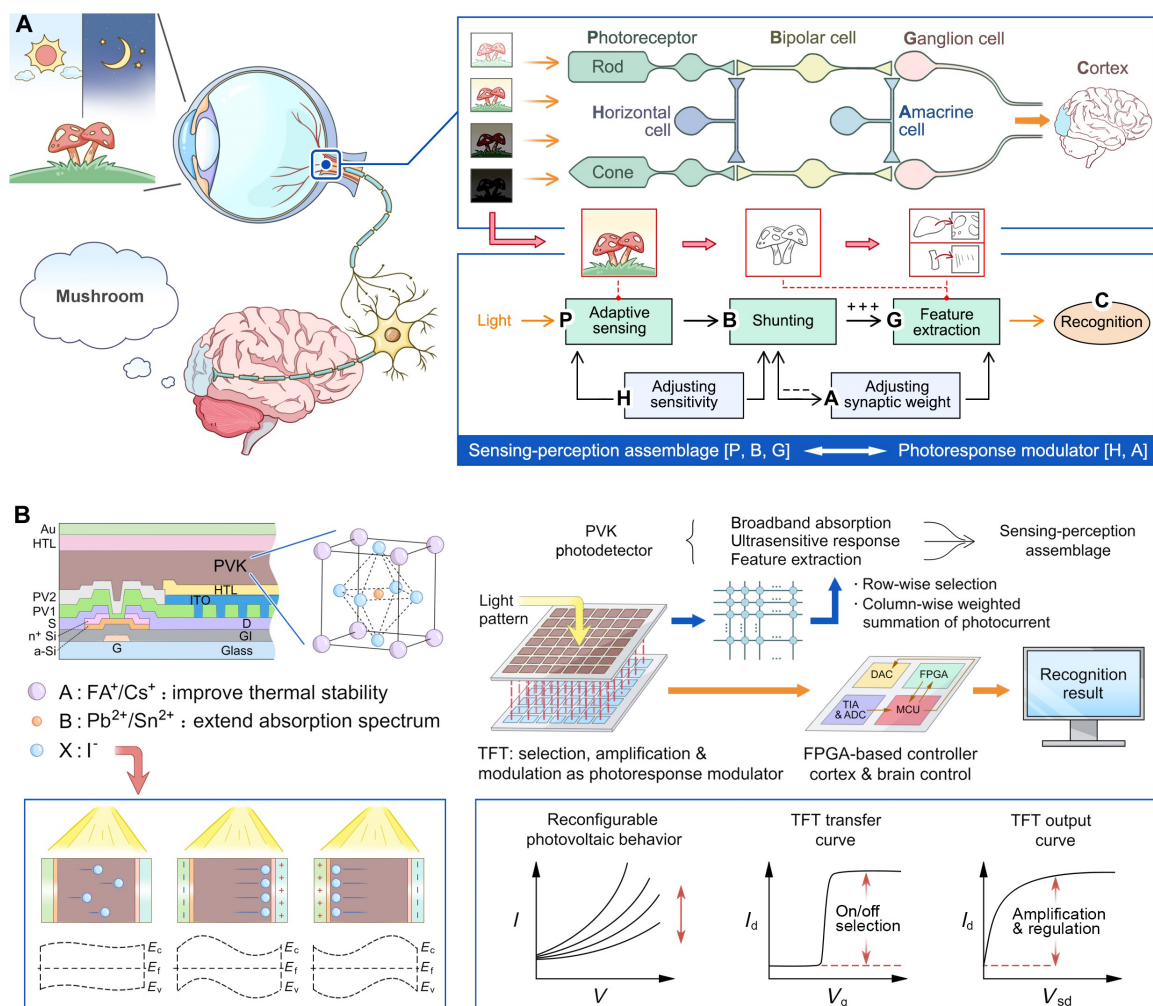
Fig. 1. Biological visual system and perovskite retinomorphic computing system. (**A**) Adaptive sensing-perception by the biological visual system through the hierarchy of photoreceptors, horizontal cells, bipolar cells, amacrine cells, and ganglion cells. (**B**) Schematic illustration and working principle of the retinomorphic computing system based on a 4096-pixel 1T-1PD perovskite RSA, microcontroller unit (MCU), and field-programmable gate array (FPGA). ADC, analog-to-digital converter; TIS, transimpedance amplifier; DAC, digital-to-analog converter.

source-drain manipulation (bottom right of Fig. 1B). On one hand, amplification of the perovskite photoresponse can enhance the quality of image sensing under dim-light conditions. When a visual object is projected onto the 4096-pixel RSA, adaptive imaging over a broad spectrum will be performed by a TFT-modulated perovskite photodetector layer. On the other hand, regulation of devices' photoresponsivities allows synaptic weight updating according to the ex situ trained sensor neural network algorithm. As such, feature extraction can be executed in the perovskite photodetector array directly by optoelectronic MAC operation during photoelectric conversion, through row-wise selection by TFT and bit line readout of the weighted photocurrent summation according to $I_m = \sum_{n=1}^{N} P_{mn} \cdot R_{mn}$, where R_{mn} is the photoresponsivity of the mth perovskite device in the nth word line and P_{mn} denotes the optical intensity irradiated onto the device (top right of Fig. 1B). Last, using a commercial microcontroller unit (MCU) and a field-programmable gate array (FPGA) as the brainoid cortex to control the execution of sensory neural network algorithms, a retinomorphic computation hardware that reproduces the complete

anatomic hierarchy of the biological vision system with full functionalities of simultaneous optical sensing, visual processing, and decision-making in a compact computing-in-sensor mode is established.

Perovskite RSA and reconfigurable photodetecting characteristics

Figure 2 (A to E) depicts the circuit layouts and a photograph of the 64 by 64 TFT panel, as well as images of a perovskite-coated TFT panel, a monolithically integrated 1T-1PD RSA, and a flexible printed cable bonded sample. Zoom-in examination reveals that each pixel of the RSA has an overall area of 500 μm by 500 μm, while the interdigitated source-drain electrode pair defines a channel width/length of 100 μm/10 μm, respectively (Fig. 2A). The TFT drain is connected to a 300 μm–by–300 μm ITO plate through SiN$_x$ vias, which serves as the bottom electrode of the perovskite photodetector. The RSA therefore has a commendable pixel fill factor of 0.36 that favors high areal efficiency of photoelectric conversion and guarantees full-hardware implementation of the retinomorphic computing
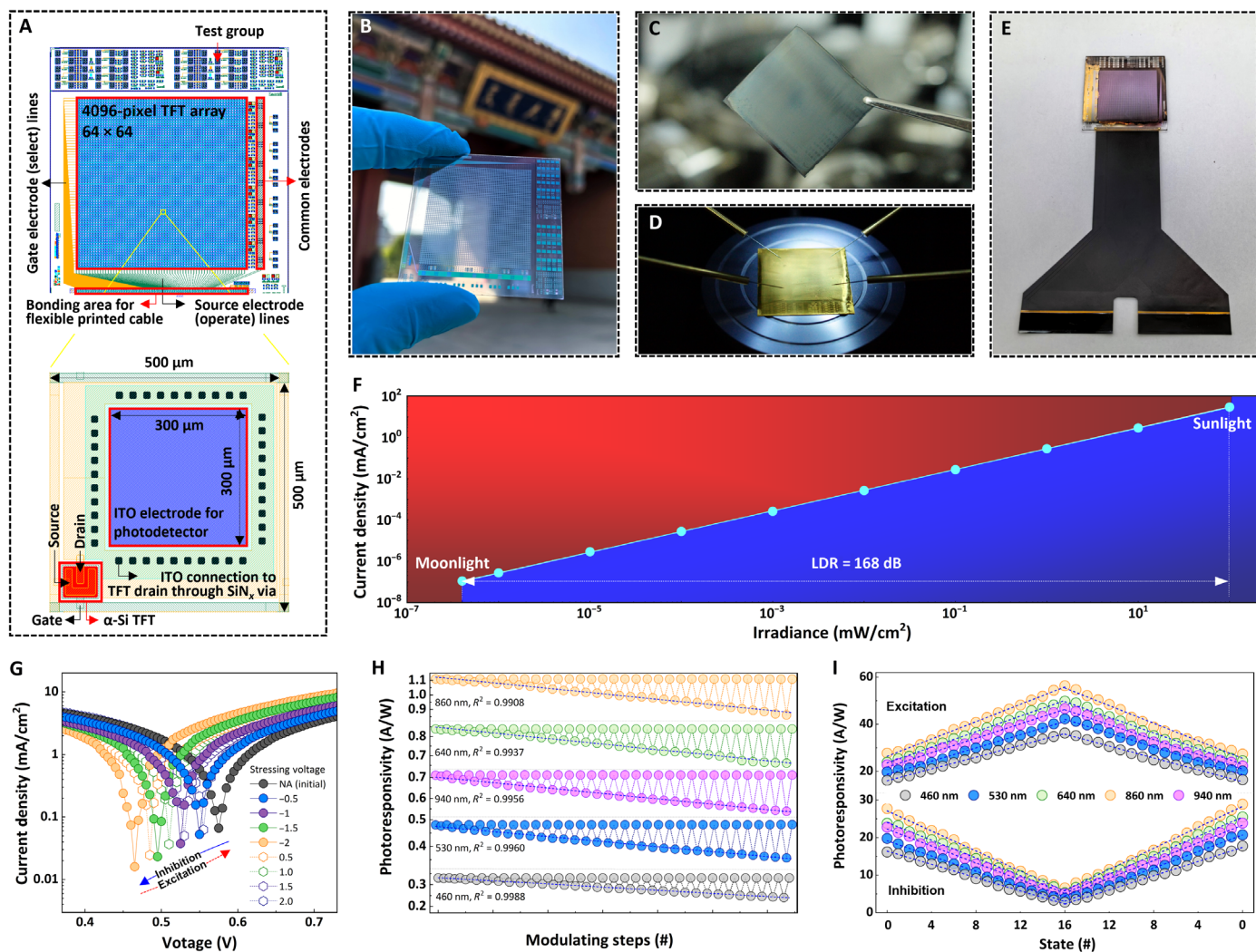
Fig. 2. The 4096-pixel perovskite RSA and its reconfigurable photodetecting characteristics. (**A**) Circuit layouts and (**B**) a photograph of a 64×64 a-Si TFT panel. Images of (**C**) a PEDOT:PSS/$FA_{0.8}Cs_{0.2}Pb_{0.5}Sn_{0.5}I_3$-coated TFT panel, (**D**) a full-structure 1T-1PD RSA, and (**E**) a flexible printed cable bonded sample. LDR (**F**) and reconfigurable photovoltaic characteristics (**G**) of an individual $FA_{0.8}Cs_{0.2}Pb_{0.5}Sn_{0.5}I_3$ photodetector recorded under standard AM 1.5G illumination, upon being subjected to voltage biases between ± 0.5 and ± 2.0 V. Broadband, linear, and reversible photoresponsivity reconfiguration of (**H**) an individual $FA_{0.8}Cs_{0.2}Pb_{0.5}Sn_{0.5}I_3$ photodetector and (**I**) a 1T-1PD pixel of the RSA under 8-mW/cm^2 monochromatic illuminations, respectively. NA, not applicable.

paradigm through 4096-pixel integration (note S2). In this work, the 4096-pixel TFT panel was designed and taped out from Tianma standard G4.5 6-mask fab and is semitransparent (Fig. 2B and figs. S4 and S5). The perovskite film has a dark brown color that endows itself strong absorption in the VIS-NIR spectrum (Fig. 2C). Upon depositing the superincumbent electron transporting layer (ETL) of C_{60} and BCP, a universal Au electrode is formed over the entire array and acts as a common terminal for all perovskite photodetectors during the photoresponsivity modulation and photocurrent readout operations (Fig. 2D). To avoid potential voltage cross-talking and misoperation by the adjacent TFTs, the photodetectors of the neighboring pixels are isolated from each other with a physical separation of 150 μm, as defined by the patterned PEDOT:PSS hole transporting layer (HTL) through aqueous etching.

The fundamental photoelectric performance of the perovskite material is first evaluated in 0.08-cm^2 individual devices (note S3 and figs. S6 to S11). With an inverted configuration of ITO/

PEDOT:PSS/$FA_{0.8}Cs_{0.2}Pb_{0.5}Sn_{0.5}I_3$/$C_{60}$/BCP/Au having an optimized 800-nm perovskite thickness, an interfacial energy barrier, and a balanced hole/electron mobility, the perovskite photodetector shows a low zero-biased dark current density (J_d) of 1.73×10^{-9} A/cm^2 in the current density–voltage (*J-V*) curves (fig. S8). The maximum external quantum efficiency (EQE), photoresponsivity (*R*), and specific detectivity (D^*) reach 90%, 0.56 A/W, and 9.11×10^{12} Jones in the VIS-NIR range of 400 to 1000 nm, rendering a high light/dark current ratio of 10^7 under AM 1.5G illumination. In particular, the perovskite device has a large LDR of 168 dB over the wide white light intensity range of 0.1 W/cm^2 to an extremely low detection limit of 0.4 nW/cm^2 (Fig. 2F), which is essential for sensitively capturing a shadowy target in a complex lighting environment (*40*). Transient photocurrent (TPC) measurement reveals that the perovskite photodetector has an ultrafast photocurrent responding speed of 2.75 ns that is favorable for instant image sensing (fig. S9), while both the 200-hour stability under continuous solar irradiation

or heating and the 30-day retention of ~96% photodetecting capability allow long-term operation for practical application (fig. S11). All these figures of merits of the perovskite device, outdistancing those of the state-of-the-art retina-inspired sensors, establish basic characteristics for ultrasensitive image sensing.

To verify the possibility of modulating the photoresponsivity of the $FA_{0.8}Cs_{0.2}Pb_{0.5}Sn_{0.5}I_3$ devices, voltage stimuli with the amplitudes of ±0.5 to ±2.0 V and a duration of 30 s were applied through the Au top electrode to induce ion migration toward the counter electrode in the perovskite layer. The universal bottom ITO electrode was grounded during measurements, while the photocurrents of the device were immediately scanned under white light illumination after the application of the stressing voltages. In response to the intensified band bending of the perovskite photodetector, the J-V curves shift obviously and continuously to a lower voltage region upon being subjected to negatively biased voltage stimuli (Fig. 2G). As the amplitudes of the stressing voltages increase from -0.5 to -2.0 V, the V_{OC} decreases from 0.58 to 0.47 V, accompanying a simultaneous decrease in photocurrent minimum from 5.28×10^{-2} to 1.61×10^{-2} mA/cm^2, respectively. It indicates that giant switching in the photovoltaic characteristics occurs in the perovskite photodetector. When the polarity of the stressing voltage stimuli is reversed, the J-V curves shift back continuously to their initial position. The open-circuit voltages, as well as the corresponding photocurrents, also become fully recovered. Therefore, reversible reconfiguration of photoresponsivity may be made possible by electric field–induced ion migration in the $FA_{0.8}Cs_{0.2}Pb_{0.5}Sn_{0.5}I_3$ photodetector. Note that the cationic nature of the $PEDOT^+$ components in the HTL layer may help in reserving the migrated I^- anions; thus, the photoresponsivity modulation is more effective and reliable by applying negative voltages onto the top Au electrode to induce iodine ion migration toward the bottom ITO electrode first.

The monochromatic photoresponsivity of the device can be modulated consecutively, linearly, and reversibly by voltage pulse trains over the VIS-NIR spectrum (note S4). As shown in figs. S12 and S13 and Fig. 2H, the $FA_{0.8}Cs_{0.2}Pb_{0.5}Sn_{0.5}I_3$ device exhibits an initial photoresponsivity of 1.11058 A/W under 860-nm illumination with an optical power of 8 mW/cm^2. When a voltage pulse with the amplitude of -0.60 V and a duration of 30 s is applied onto the device, its photoresponsivity decreases to 1.11056 A/W. Afterward, application of a 2.0-V voltage can return the device to the initial photoresponsivity state. Then, a voltage pulse with the amplitude of -0.625 V and a duration of 30 s switches the device photoresponsivity to 1.10045 A/W, which can be recovered to the pristine value by the subsequent 2.0-V voltage stressing. Similarly, the application of negative voltage pulses with the ramping step of -0.025 V and a duration of 30 s can program the photoresponsivity of the perovskite device continuously and linearly to 0.89247 A/W, while the following 2.0-V voltage stress can completely reset it to the initial value with full reversibility. Such linear and reversible modulations of the $FA_{0.8}Cs_{0.2}Pb_{0.5}Sn_{0.5}I_3$ device photoresponsivities are observed over all the wavelengths of 940, 860, 640, 530, and 460 nm, again confirming the effectiveness of the ion migration–based reconfiguration strategy. Note that the reconfigurable photoresponsivity of the perovskite device can retain even after 10,000 cycles (fig. S14), further confirming the excellent reliability and stability and benefiting to the long-term operation for practical application. Critically, a large photocurrent/dark current ratio exceeding 9×10^3 can be maintained over all wavelengths after photoresponsivity reconfiguration, which in turn allows high-contrast image sensing in dim-light

environments. Multiplying the device current (8.24×10^{-7} A under 860-nm irradiation), the reading voltage (1.6 V), and the responding speed (2.75 ns), the perovskite-based photovoltaic detector exhibits an ultrasmall energy consumption of 3.63×10^{-15} J, which is close to the biological neuronal system (10 fJ per synaptic event). Although passivation of perovskite with organic small molecules may further enhance the device photodetecting capability, it also hinders photoresponsivity reconfigurability for retinomorphic computing. Thus, in this work, passivation of perovskite is not used.

When incorporated into 1T-1PD pixels, the large on/off ratio of the a-Si TFT will select the target $FA_{0.8}Cs_{0.2}Pb_{0.5}Sn_{0.5}I_3$ device properly for subsequent operation (note S5). The source-drain manipulation may further regulate the sensor device's photoresponse through ion migration. As shown in Fig. 2I, when a gate voltage of 10 V and a source voltage of -4.0 V are used, the monochromic photoresponsivities of the pixel are 22.37, 27.38, 24.52, 20.18, and 16.42 A/W, respectively, recorded under illuminations at the wavelengths of 940, 860, 640, 530, and 460 nm with the optical intensity of 8 mW/cm^2. By continuously applying voltage pulses through a source electrode with a ramping step of -0.2 V and a duration of 10 s, pseudo-linear enhancement of the pixel's photoresponsivities to 46.67, 56.35, 49.78, 41.38, and 35.78 A/W is achieved over 16 steps with linearities of more than 0.99 at all experimental wavelengths (table S2). It emulates the excitory modulation of the photoreceptors inside biological retina. Note that these photoresponsivities, over 100 times higher than most of the state-of-the-art retinomorphic devices (13–28), guarantee ultrasensitive image sensing in a dim-light environment. Again, a commendable on/off ratio of 200 can be maintained in the 1T-1PD geometry. Upon reversing the polarity of the voltage stimuli and decreasing their amplitude from 3.5 to 2.0 V with a ramping step of -0.1 V, the photoresponsivities of the pixel become linearly, symmetrically, and almost fully recovered to their pristine values, with linearities of ~0.99 over all five wavelengths. Linear reversible inhibition of the responsivities to 5.08, 6.59, 5.31, 3.81, and 2.80 A/W is also observed when voltage stimuli with the ramping step of -0.1 V from 2.0 to 3.4 V and a duration of 10 s are applied in 16 modulation steps. Such linear, fully reversible inhibitory and excitory modulations not only allow precise updating of synaptic weight for weighted MAC operations but also solve the paradox of simultaneously achieving ultrasensitive and reconfigurable photoresponsivity for high-fidelity retinomorphic computation.

Adaptive image sensing performance

The ultrasensitive, broadband image sensing capability of the monolithically integrated 4096-pixel perovskite RSA was first assessed using a commercial readout circuit. In our experiment, the gate voltage is set to 10 V for pixel selecting via row-wise scanning, while a source voltage of 0.1 V is applied through bit lines in a column-by-column manner to read the pixel's current response with the Au common electrode (note S6). As shown in Fig. 3 (A to D), fig. S19, and movie S1, the 1T-1PD pixels of the RSA exhibit an average dark current of 1.80 nA and average photocurrents of 11.84, 50.12, 91.47, and 181.37 nA under white light illuminations of 10, 50, 0.10, and 0.20 mW/cm^2, respectively. By defining a particular pixel outputting photocurrent lower than 90% of the average value as dead pixel, a high production yield of 99.88% can be derived from the photocurrent mapping profiles for the present perovskite RSA. In addition, the monolithically integrated RSA has a high pixel-to-pixel uniformity (PPU) exceeding 95.82%, which is comparable to those of the
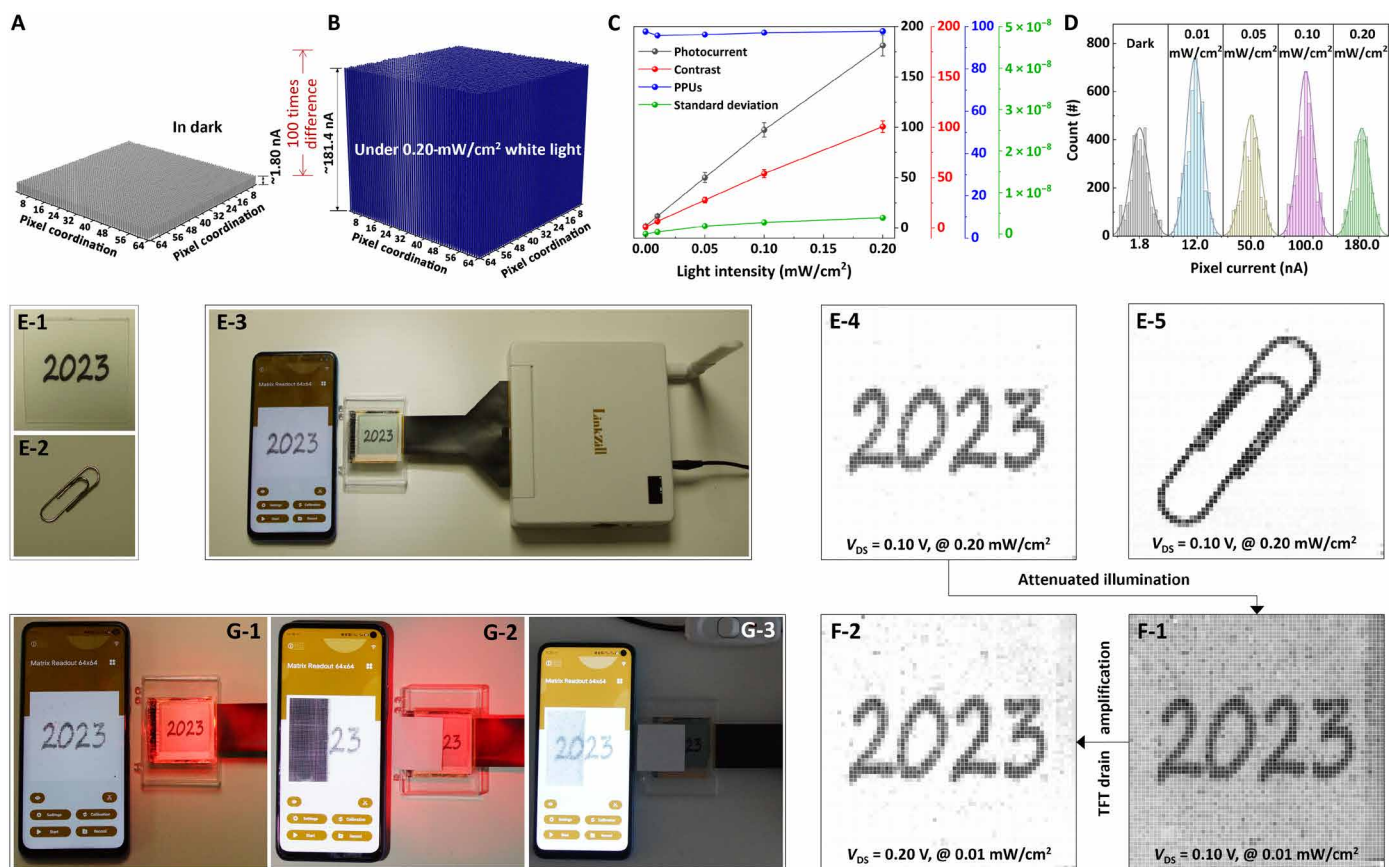
Fig. 3. Adaptive image sensing performance of the 4096-pixel perovskite RSA. (**A**) Dark and (**B**) photo current profiles of all pixels in the RSA. (**C**) Average values, variations, pixel-to-pixel uniformities, photo-to-dark ratios, and (**D**) distributions of pixel currents recorded under various white light intensities. (**E**) Image sensing of handwritten digits 2023 and a metallic paper clip with the perovskite RSA and a commercial readout circuit under 0.20-mW/cm² white light illumination. (**F**) Adaptive sensing of handwritten digits 2023 under 0.01-mW/cm² white light illumination before and after photoresponsivity amplification, respectively. (**G**) Image sensing of handwritten digits 2023 under VIS-NIR monochromic illuminations before and after being partially sheltered by a piece of print paper, respectively.

state-of-the-art visible light, infrared, and x-ray photodetectors (*41–45*). High PPU will help to increase the signal-to-noise ratio, lowering the deviation of the interpixel contrasts and improving the spatial resolution of the RSA.

As shown in Fig. 3E, fig. S20, and movie S2, handwritten digits and letters printed on transparent plastic sheets, as well as entities of a metallic paper clip, a key, and a hairpin, can be faithfully captured by the perovskite RSA with source and gate voltages of 0.1 and 10 V, under 0.20-mW/cm² white illumination that is much weaker than normal room light conditions. In this situation, the imaging contrasts of the RSA, which is defined as the current ratio of the pixels occupied by the target and the blank background, reach as high as 74.71. It corresponds to a photoresponsivity of 0.36 A/W. On the other hand, although the pixel's photocurrent and thus the photo-to-dark current ratio decrease at low optical intensities, the constant photoresponsivity over wide illumination power (LDR) range of the perovskite photodetector still allows clear imaging of the visual targets by the RSA under dim-lit conditions. Figure 3F-1 and fig. S21 (B and C) summarize the images of handwritten digits acquired under various white light illumination intensities of 0.01, 0.05, and 0.10 mW/cm² and a source voltage of 0.1 V, respectively. At all optical intensities, the handwritten digits "2023" can be visualized clearly (movie S3). The corresponding average current contrasts of the

target and background pixels are 5.96, 21.76, and 40.99. Note that the lowest light intensity of 0.01 mW/cm² is approaching that of the moonlight in the evening, confirming the perovskite RSA's capability of capturing indistinct targets in caliginous environments. In addition, the ratio of the pixels occupied by the handwritten digits in the acquired images and in the original template is defined as image sensing fidelity of the RSA. Through counting the occupied pixels in Fig. 3 (E-4 and F-1) and fig. S21 (B and C), high fidelities exceeding 96% under all illumination intensities are demonstrated (fig. S21E).

Since source-drain modulation of the perovskite device's internal ion distribution and potential profile can substantially reconfigure its photoresponsivity, image sensing quality under low optical powers will be greatly improved. When a source voltage of 0.2 V is applied, the pixels' photoresponsivities and imaging contrast of handwritten 2023 acquired under 10-μW/cm² illumination are amplified by 618.49% to 2.93 and 36.88 A/W, respectively (Fig. 3F-2; fig. S21, C and D; and movie S4). The image contrast is close to that obtained under 10 times stronger illumination intensity of 0.10 mW/cm² without amplification, verifying the present RSA's capability of executing adaptive image sensing tasks. Remembering that ultrahigh photoresponsivity reaching 50 A/W can be achieved upon TFT-enabled RSA reconfiguration, enhancements of extreme dim-lit imaging quality to that obtained under normal

daylight illumination can thus be reasonably expected with larger source voltages.

Because of the broadband absorption characteristic of the NBG perovskite $FA_{0.8}Cs_{0.2}Pb_{0.5}Sn_{0.5}I_3$, image sensing under monochromic illuminations over the entire visible and short wavelength NIR spectrum is also demonstrated by the perovskite RSA. As shown in Fig. 3G, fig. S22, and movie S5, the handwritten digits 2023 can be captured clearly under 0.20-mW/cm^2 monochromic illuminations at the wavelengths of 460, 530, 640, and 860 nm, with the corresponding imaging contrasts of 64.68, 73.35, 84.60, and 81.71%. The NIR imaging capability of the perovskite RSA, in addition, also enables visualizing targets behind thin obstacles. When a piece of printing paper is covered on the handwritten digits "20," they can still be visualized by the RSA under 860-nm irradiation (Fig. 3G-3 and movie S6). In comparison, when illuminated with a 640-nm light source, the handwritten digits 20 cannot be imaged anymore. Such NIR detection is of great importance for airport or railway station security surveillance, as well as offers possibility of building night vision systems and realizing intelligent medical diagnosis.

Hardware implementation of retinomorphic computation system

Last, we demonstrate all-hardware implementation of a retinomorphic computation system using the 4096-pixel perovskite RSA, MCU, and FPGA controllers. Now, lightweight CNNs such as LeNet-5 are most popularly used for the simulation of retinomorphic computing with advanced sensor devices. Facilitated by sharing of the convolutional kernel parameters, CNNs allow for end-to-end learning of the grid-like pixel feature with relatively modest computing cost. Nevertheless, although the first layer of convolution can be implemented by optoelectronic MAC operations in the RSA by $I_i = \Sigma P_l \times R_l$, where P_l and I_i represent the input light intensity and output photocurrent, while R_l is the photoresponsivity of the array pixel, pooling and further convolution using the current representatives of the extracted features (outputs of the first convolution layer) as inputs cannot be performed by the same way on the RSA any more (note S7 and fig. S23A). As such, the effectiveness of extracting sufficient features using the optoelectronic sensor devices and a single layer convolution operation for high-accuracy target recognition is limited, which restricts the power of CNNs for handling complex images. On the other hand, to extract finer local features during the first layer convolution, the stride is often set smaller than the dimension of the convolution kernel (fig. S23B). After executing MAC operation with the incident light pattern during the optoelectronic sensing process, the small-step shift of convolution kernel will result in rewriting of the pixels' photoresponsivities in the overlapped regions according to the pretrained neural network algorithm. This not only addresses a high criterion for the device endurance but also requires repeated snapshots and processing of the visual target over the rewritten pixels during convolution to accomplish a feature extraction task. The multiple-time "see, write, and calculate" operations do not conform with the instantaneous "see and recognize" principle of biological visual systems and seriously affect the overall performance of the retinomorphic system. Developing a more efficient feature extraction method that can be completely and simultaneously executed during the image sensing process while encodes as much information as possible from the generic representation of the captured visual scenario is thus a basic requirement to achieve highly effective retinomorphic computing based on advanced optoelectronic sensor devices.

In this study, we design a ODFE algorithm and combine it with a fully connected (FC) layer into a fast optical-based pattern recognition network (FOPR-Net) to fulfill the above requirements (Fig. 4A). Here, a 64×1 weight vector $\mathbf{W}$ is designed, pretrained, and mapped repeatedly onto each column of the photoresponsivity matrix of the 64×64 perovskite RSA. When incident light patterns are projected onto the RSA, multiplication between pixel's light intensity and photoresponsivity occurs simultaneously over the entire array during the photoelectric conversion (thus image sensing) procedure. Column-wise summation of the weighted photocurrents equals the MAC operation, resulting in one-time readout of a 1×64 vector $\mathbf{I}$ [$\mathbf{I}_1, \mathbf{I}_2 \ldots \mathbf{I}_{64}$] in which each element reflects the corresponding column feature of the visualized light pattern. Then, the extracted features are fed into the FC layer to deliver a final recognition result through simple spatial information pooling and forward propagation operation.

Ex situ training of FOPR-Net was conducted in a common PyTorch framework through initialization, forward and backward propagations, according to the gradient descent scheme of the L2 loss function for synaptic weights updating (note S7). The synaptic weights in the 1D vector are quantified into either positive or negative decimal numbers with 5-bit precision, which are in accordance with the 32-state reconfigurable photoresponsivity potentiation and depression characteristics of the 1T-1PD perovskite RSA. A subset of 50,000 handwritten digit image samples is extracted from the Modified National Institute of Standards and Technology (MNIST) dataset for the network training. Figure 4 (B and C) and table S3 plot the synaptic weight and aligned photoresponsivity vectors obtained after 30 training epochs. Using the training-ready weight vector, FOPR-Net can recognize a testing subset of 10k MNIST handwritten digit images with a commendable accuracy of 88.7% (Fig. 4, D and E, and fig. S25). As shown in Fig. 4F, the successful classification of arbitrary handwritten digit sample confirms the effectiveness of the ODFE and FOPR-Net algorithms.

Figure 4G displays the prototype of the retinomorphic computing hardware system constituting a 4096-pixel perovskite RSA, a home-made printed circuit board (PCB), and a commercial FPGA controller. The RSA serves as an image sensing panel and an instantaneous feature extractor in the system, while the FPGA controller accounts for information pooling of the FOPR-Net algorithm. On the other hand, the PCB containing MCU and periphery modules controls line selection, weight writing, and data reading of the RSA. Before operating, the photoresponsivities of all pixels are programmed in one-shot according to the pretrained weight vector. Then, a handwritten digit drawn with a black marker pen on a piece of transparent plastic sheet is used and placed on top of the RSA as a visual target to assess the pattern recognition performance of the retinomorphic hardware. As controlled by the MCU driver, the RSA collects and extracts features from the incident light patterns shielded by the handwritten digit template and amplify and feed them as a 1D voltage vector into the following FC layer. By running FOPR-Net manipulation of the image feature on the RSA and the FPGA board, handwritten digits of 0 to 9 can be visualized and recognized in real time, with their clearly captured images and recognition outputs displayed as the standard Arabic numbers on the embedded liquid crystal display (LCD) screen (Fig. 4H, fig. S26, and movies S7 and S8). During the experiment, 100 sets of MNIST handwritten digit images are input randomly into the system, which can be processed within 0.54 s to deliver their recognition results. Therefore, the overall response speed of the present retinomorphic system is taken as
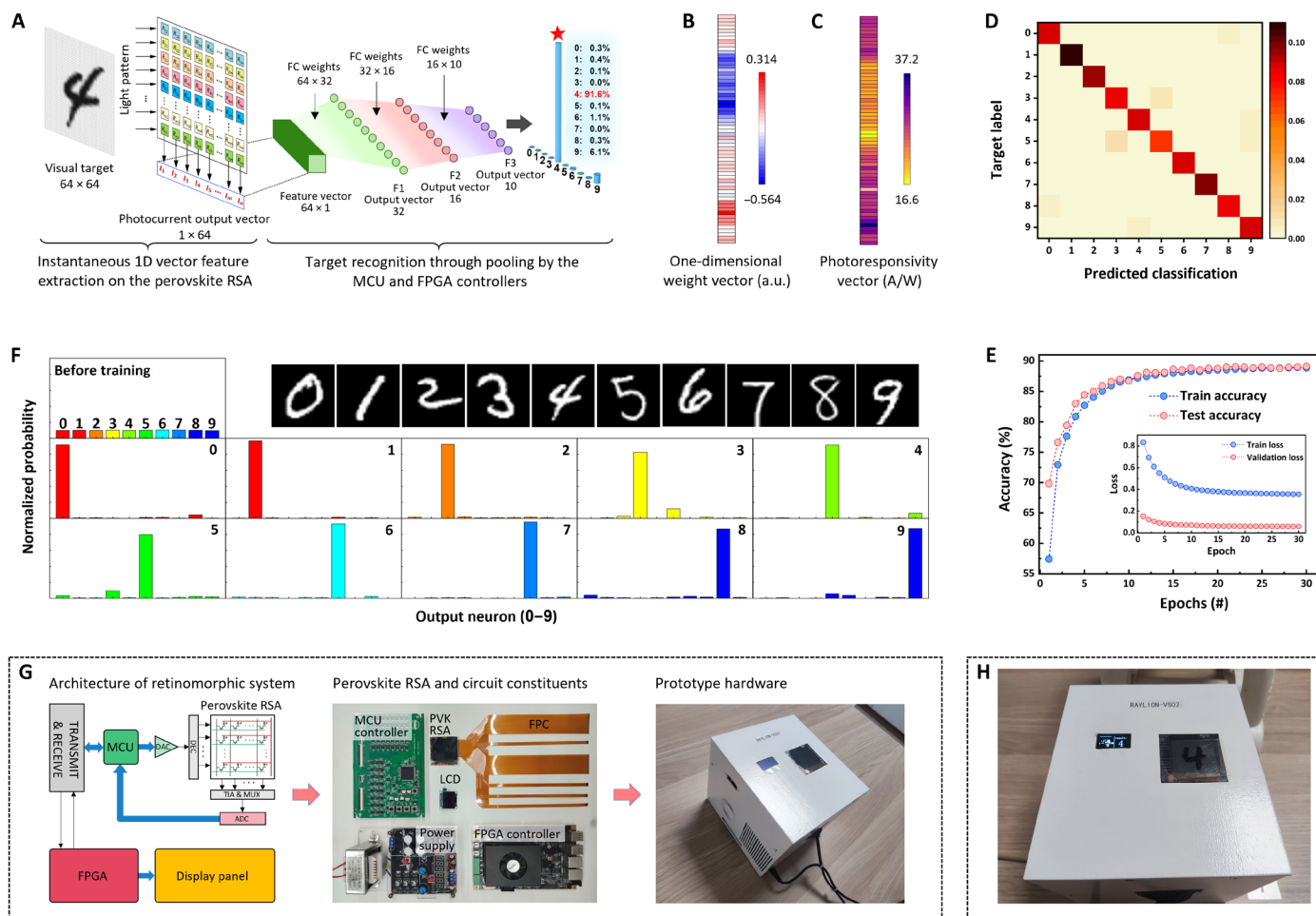
Fig. 4. Hardware implementation of perovskite-based retinomorphic computing system. (**A**) FOPR-Net for instantaneous ODFE through the perovskite RSA and target recognition through pooling by the FPGA-based FC neural network. Training-ready (**B**) 1D synaptic weight vector, (**C**) aligned photoresponsivities, (**D**) confusion matrix, (**E**) evolved recognition accuracy, and (**F**) simulated recognition results for MNIST handwritten digit database. (**G**) Architecture and photographs of the complete prototype of perovskite RSA-based retinomorphic hardware system. (**H**) Captured image and recognition outcome of handwritten digit "4" acquired by the perovskite RSA-based retinomorphic hardware system. a.u., arbitrary units.

5.4 ms per frame or 184 frames/s (fig. S27). Note that the retinomorphic system uses a home-made PCB to read feature information from the RSA, and the analog-to-digital conversion of the extracted feature information is probably the speed-limiting step during operation. Therefore, while the photocurrent response of the perovskite photodetector is as fast as in a range of ~100 ns, practical limitation in data transfer now defines the achievable speed for full system operation. Furthermore, optimizing the readout circuit of the RSA may accelerate the responding speed of the retinomorphic system, which is yet beyond the scope of the present work.

Embodied intelligent vision for locomotion control of exoskeleton robot

Such retinomorphic hardware can arm an exoskeleton robot with the ability of sensing, recognizing, and responding to environmental information intelligently and assist people with physical disabilities to live an easier life. For instance, when passing through crossroads, pedestrians can use their vision to observe the changing traffic lights with a flashing counting down timer, based on which they are able to

make decisions and pace accordingly. For patients with blindness and dyskinesia, on the other hand, these actions can be performed by an exoskeleton robot with embodied intelligent vision instead (Fig. 5A). In this work, we assume that an exoskeleton robot moves at the initial constant speed of 1.0 m/s, while its maximum speed should be limited to slower than 2.5 m/s. When it approaches to 5 m away from the crossroad, the retinomorphic system starts to monitor the counting down numbers of the flashing timer continuously in a 1-s interval. The premounted ODFE algorithm simultaneously decomposes the observed 64 × 64 pixels flashing numbers into a 64 × 1 feature vector, which is then recognized with a temporal network to decide the robot's next-step motion status by considering the spatiotemporal relationship between the counting down time, moving speed, and distance from the traffic junction. Since the exoskeleton robot can pass the crossroad within 5 s at its initial speed, it only needs to walk steadily when the monitored 5-s counting down numbers are in the series from [9, 8, 7, 6, 5, 4], [8, 7, 6, 5, 4, 3], to [5, 4, 3, 2, 1, 0] (left of Fig. 5B). If the flashing timer counts down from 4 or 3, it indicates that the exoskeleton robot has to speed up to cross the junction. In this case,
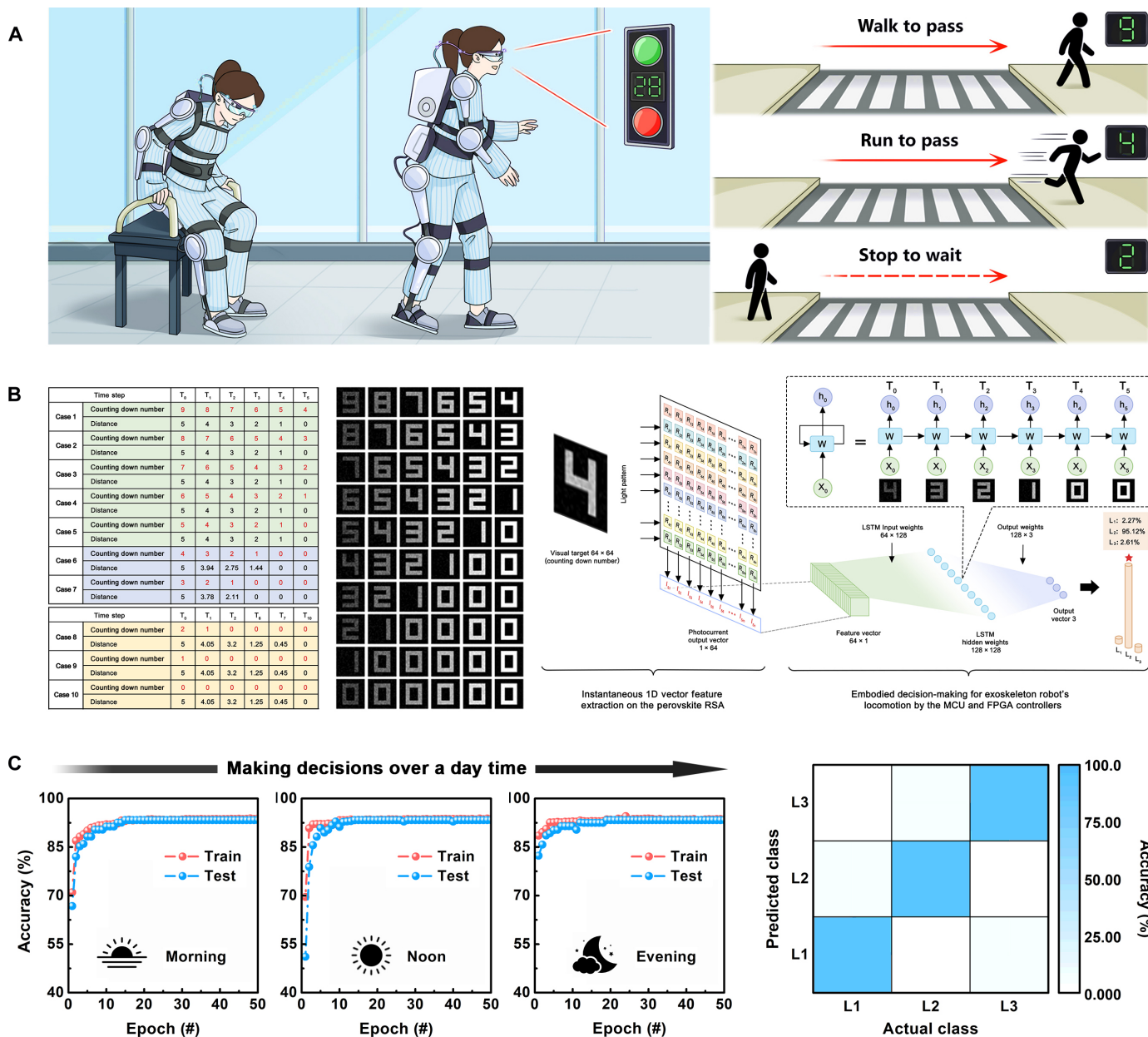
Fig. 5. Embodied intelligent vision for exoskeleton robot's motion control. (**A**) Schematic illustration of a retinomorphic computing system armed exoskeleton robot to assist patients with blindness and dyskinesia to pass through the traffic junction safely. (**B**) Motion scheme (left), database examples (middle), and FO-RNN (right) for the exoskeleton robot according to various monitored counting down numbers of the flashing timer. (**C**) Accuracies (left) and overall confusion matrix (right) of making decisions for the exoskeleton robot to pass through the traffic junction safely during different periods of a day.

the acceleration and the final speed should be no less than ($1/8$ m/s^2, 1.5 m/s) and ($4/9$ m/s^2, $7/3$ m/s), respectively. When the counting down timer flashes from 2, 1, or 0, the exoskeleton robot in no way can pass through the traffic junction safely under the limiting speed of 2.5 m/s. Thus, it should decelerate to stop at the stop line and wait for the traffic light to turn into green again, with the deceleration speed of no less than -0.1 m/s^2. The detailed calculation process for the above motion scheme of the exoskeleton robot is summarized in note S8.

To train the retinomorphic computing system to accomplish the above-mentioned exoskeleton robot tasks, we design a fast optical-based recurrent neural network (FO-RNN) comprising an input layer, a ODFE layer, a long short-term memory (LSTM) hidden layer, and an output layer with three neurons of L_1 to L_3 that represent the three motion statues of the exoskeleton robot when approaching the crossroad (right of Fig. 5B). In particular, the LSTM layer involves six continuous time steps of T_0 to T_5, according to the robot's motion scheme that requires at least 5 s to pass the traffic junction from the distance of 5 m at the initial constant speed of 1 m/s. In each step, a 64×1 feature vector (x_0 to x_5) of the standard electronic counting down digit monitored at the present time is input and processed to result in an updated hidden state ($h_0 \sim h_5$) of

the step. The hidden state contains information of the previous time step, which will be fed into the next time step upon updating. A recognition label of the counting down number monitored at the present time is output at each time step. These labels obtained at the steps of T_0 to T_5 are temporally correlated with each other and combined into a six-member group by the LSTM to deliver the final probability of outputting motion statues of L_1 to L_3. The robot will pace correspondingly to maintain the traffic safety.

Here, we compose a database with images of standard electronic digits in a black ground, showing different contrasts and noise levels to represent the counting down numbers of the flashing timer that are recorded in different light conditions for FO-RNN training (middle of Fig. 5B and figs. S28 and S29). Since the counting down numbers are monitored continuously with a time interval of 1 s as the robot approaching to 5 m away from the crossroad, each subgroup of the database should contain six images of electronic digits that are arranged in a monotonically decreasing sequence. It also corresponds to the six time steps of the LTSM hidden layer. Note that each image contains dual labels of the counting down number itself and motion statues of L_1 to L_3. As discussed previously, the motion labels are L_1, L_2, and L_3, when the numbers recorded in the T_0 images are in the range of (9 to 5), (4 to 3), and (2 to 0), respectively. On the other hand, the brightness of the counting down number and thus the electronic digit increase as the robot moves nearer to the junction. In the case that the counting down number decreases to 0 at a certain moment, all the following numbers will be recorded as 0. In this study, 3000 training subgroups and 300 testing subgroups of database are composed for each label of L_1, L_2, and L_3. Upon adjusting the network parameters with the back-propagation algorithm and the Adam optimizer, the deviations between the predictions and labels are minimized. As shown in Fig. 5C and fig. S30, the FO-RNN has high accuracies of 93.33% for different time periods over a day, which allows the retinomorphic computation system and the exoskeleton robot to assist a patient to pass through the traffic junction safely.

DISCUSSION
In summary, we implement the retinomorphic computing hardware with a 4096-pixel perovskite image sensor array. It not only surpasses the performance of the existing retinomorphic sensor devices in terms of reconfigurable photoresponsivity and large-scale integrating capability but also demonstrates a technically more feasible solution to turn the fascinating concept of embodied intelligent vision into reality (Table 1). Through merging the real-time predictable visual information to understand environmental perception and infer entity actuations, such retinomorphic computing hardware is of undoubted importance in areas of exoskeleton robots, autonomous vehicles, etc. Upon maximizing the complexity and range of tasks that an embodied intelligent vision system can perform, the instantaneous see, recognize, and respond capability may also enable all-weather fast actuation of mobile robots including pilotless automobile to detect and dodge on-road pedestrians, accompanying vehicles and other traffic obstacles. Along with this motivation, future efforts should be devoted to miniaturizing the retinomorphic pixels into a sub-10-μm dimension, fabricating with flexible substrates, integrating them into high resolutions such as 640 × 480 pixels, as well as encapsulating with optical lenses and complementary metal-oxide semiconductor auxiliary components into chiplets for practical applications.

MATERIALS AND METHODS
Precursor and perovskite preparation
Formamidine iodide (FAI; 99.999%) was provided by Greatcell Solar company. CsI (99.999%), PbI$_2$ (99.999%), SnI$_2$ (99.999%), SnF$_2$ (99.999%), N,N-dimethylformamide (DMF; 99.8%), dimethyl sulfoxide (DMSO; 99.8%), chlorobenzene (99%), and BCP were purchased from Sigma-Aldrich. PEDOT:PSS (Clevios P VP. AI 4083) and C$_{60}$ were obtained from Heraeus and Nano-C Company, respectively. PEDOT:PSS was filtrated with a 0.22-μm syringe filter before use. Precursor solutions of NBG perovskite FA$_{0.8}$Cs$_{0.2}$Pb$_{0.5}$Sn$_{0.5}$I$_3$ with the concentrations of 1.4 to 1.8 M were prepared in a nitrogen-filled glove box, through dissolving 1.12 mol of FAI, 0.28 mol of CsI, 0.7 mol of PbI$_2$, 0.63 mol of SnI$_2$, and 0.07 mol of SnF$_2$ in 0.78- to 1-ml mixed solvents of DMF:DMSO (with a volume ratio of 9:1) and stirred for 12 hours. All other chemicals and reagents were used as purchased.

Device fabrication
Perovskite devices, with a p-i-n configuration of ITO/PEDOT:PSS/ perovskite/C$_{60}$/BCP/Au and a size of 0.08 cm^2, were fabricated first for fundamental photovoltaic performance characterization. The prepatterned ITO substrates were completely cleaned in deionized water, acetone, and isopropanol, each for 15 min in that order. The overall size of the glass substrate is 1.7 cm by 1.7 cm, while that of the patterned ITO electrode is 1.7 cm by 1.2 cm. The ITO substrates were then treated with UV irradiation to improve the hydrophilicity to assist the coating of PEDOT:PSS HTL. Subsequently, the PEDOT:PSS HTL was spin-cast onto the UV-treated ITO surface at 5000 rpm for 30 s and baked at 150°C for 15 min. Forty-microliter as-prepared perovskite precursor solutions with different concentrations were spin-coated onto the PEDOT:PSS films with a speed of 4000 rpm for 30 s to afford perovskite layers with different thicknesses of 600, 800, and 1000 nm. During the last 15 s of spinning, 180 μl of anti-solvent of chlorobenzene was added quickly onto the spinning sample. Afterward, the as-prepared sample was annealed at 100°C for 8 min to form the final perovskite film. Ultimately, the ETLs of C$_{60}$ (20 nm) and BCP (5 nm) were continually deposited onto the active layers via thermally evaporation. For the top electrode, 120-nm-thick Au pads with the active area of 0.08 cm^2 (0.2 cm by 0.4 cm) were deposited onto the ETLs through thermal evaporation. The perovskite devices were encapsulated with UV curing adhesive and a glass slide for stability measurements.

Perovskite devices with similar configurations but smaller sizes of 7.85×10^{-5} cm^2 were fabricated to verify the enhancement and reconfiguration of photoresponsivity through intrinsic ion migration effects. In this case, the ITO bottom electrode is not prepatterned, while the top circular shape Au electrodes with a diameter of 100 μm and a thickness of 50 nm were deposited via dc magneto sputtering. The size of the devices is then determined by the diameter of the Au top electrodes.

The 1T-1PD structure retinomorphic sensor was fabricated by superimposing perovskite-based photodetectors on an a-Si TFT panel. To match the electrical performance of perovskite devices, the a-Si TFTs were designed with a channel W/L of 100 μm/10 μm, a maximum driving voltage of 20.0 V, and output currents in the range of 10^{-12} to 10^{-6} A ($V_{DS} = 1$ V). The 4096-pixel a-Si TFT panels were taped out from Tianma Microelectronics Co. Ltd., while the perovskite-based photodetector array was fabricated through solution processing directly on the TFT panel. The active area of the perovskite devices, which is defined by the bottom ITO electrode connected to

Table 1. Performance comparison. The comprehensive performance of retinomorphic sensor devices and computation systems.

Photosensitive material	Device structure	Photo-responsivity (A/W)	On/off ratio	Array scale	Fill factor	Neural network type	Computation function	Full-hardware implementation	Reference
SWNT@GDY	Phototransistor	0.03	10^3	9 (3 × 3)	~0.052	Convolutional neural network	Image filtering and coding/decoding	No	(21)
WSe$_2$	Photodiode	0.06	~100	9 (3 × 3)	~0.0037	Fully connected neural network	Coding/decoding and classification	Partial	(14)
PdSe$_2$/MoTe$_2$	Phototransistor	0.31	–	64 (8 × 8)	–	Convolutional neural network	Pattern recognition	No	(18)
MoTe$_2$/graphene /poly(vinylidene fluoride-trifluoroethylene)	Phototransistor	0.83	–	9 (3 × 3)	~0.05	Convolutional neural network	Image filtering and motion tracking	Partial	(23)
NbS$_2$/MoS$_2$	Phototransistor	1.1	~30	100 (10 × 10)	~0.012	–	Denoising and motion tracking	Partial	(26)
MoS$_2$/pV3D3-PTr	Phototransistor	19.8	1.8	31	~0.27	Fully connected neural network	Image filtering	Partial	(16)
WSe$_2$/h-BN	Phototransistor	5.93×10^4	0.75	25 (5 × 5)	~0.35	Single-layer perceptron	Coding/decoding and motion tracking	Partial	(24)
Perovskite	1T-1PD	56.35	~200	4096 (64 × 64)	0.36	ODFE	Instantaneous sensing, target recognition and, decision-making	Yes	This work

the drain of the TFT, is 9×10^{-4} cm^2 (300 μm by 300 μm). To avoid potential voltage stimulus cross-talk and misoperation by the neighbor TFT devices, the highly conductive PEDOT:PSS universal HTL was patterned into isolated pixels by standard photolithography and aqueous etching processes. Before depositing, the TFT panel was completely cleaned in deionized water, acetone, and isopropanol, each for 15 min in that order. Then, it was treated with UV irradiation to improve the hydrophilicity. Considering that the total area of the TFT panel (3.2 cm by 3.2 cm) is about four times as that of the ITO substrate (1.7 cm by 1.7 cm) used for individual perovskite device fabrication, the spin-coating speed of PEDOT:PSS was decreased to 2000 rpm in this case to ensure the same HTL thickness. After annealing at 150°C for 15 min, a 0.5-ml AZ5214 photoresist was spin-coated onto the PEDOT:PSS HTL layer at the spinning speed of 1000 rpm for 10 s and 5000 rpm for 30 s, followed by baking at 100°C for 90 s. Afterward, a photomask with square-shaped openings of 350 μm by 350 μm and separations of 150 μm was placed on top of the sample. The photomask openings were right above the ITO electrodes connected to the drain of the TFT, with their centers overlapped with each other. The sample was then exposed to UV irradiation of photolithography process for 13 s and immersed in deionized water for 35 s. The exposed photoresist denatured and retained, while the unexposed part was removed. The PEDOT:PSS in the unexposed area therefore manifested. The sample was further immersed in deionized water for another 10 s to remove the manifested part of the water-soluble PEDOT:PSS layer, following by ultrasonicating with acetone to remove the denatured photoresist in the exposed part. As such, separated square-shaped islands of PEDOT: PSS with the size of 350 μm by 350 μm and a

separation of 150 μm were formed on top of the ITO electrode regions of the TFT panel. Subsequently, 180 μl of 1.8 M perovskite precursor solution was spin-coated at the speed of 3000 rpm for 30 s, while 500 μl of chlorobenzene was dropped rapidly during the last 15-s spinning process. The C$_{60}$/BCP (20/5 nm) ETL layer was continuously deposited through thermally evaporation. The 50-nm-thick top Au electrode is universally deposited through dc magneto sputtering and connected to the common electrode area of the TFT panel. Last, the monolithically integrated 4096-pixel 1T-1PD RSA was encapsulated with UV curing adhesive and a glass slide to ensure stable operation in an ambient environment.

Characterization and measurement

Thickness and optical absorption spectra of the FA$_{0.8}$Cs$_{0.2}$Pb$_{0.5}$Sn$_{0.5}$I$_3$ thin films prepared on glass substrates were measured with a Filmetrics Profilm 3D Optical Profiler and a Shimadzu UV-Visible 3600 Spectrophotometer, respectively. X-ray diffraction patterns were recorded to investigate the crystallinity of the NBG perovskite on a Bruker D8 Advance diffractometer with CuKα radiation from the diffraction angles of 5° to 40°. X-ray photoelectron spectroscopic and UV photoelectron spectroscopic measurements were performed using a Nexsa x-ray photoelectron spectrometer to determine the chemical composition, work function, Fermi level, and band positions of the perovskite film. High-resolution field-emission scanning electron microscopic (SEM) observation was conducted by a Tescan MAIA3 GMU model 2016 scanning electron microscope to acquire the morphology and grain size of the perovskite film. The SEM perovskite sample was prepared on an ITO/PEDOT:PSS substrate.

Cross-sectional scanning transmission electron microscopic (STEM) images of the TFT and perovskite photodetector were acquired using a Thermo Fisher Scientific Talos F200X microscope, wherein the STEM samples were prepared using a GAIA3 focused ion beam time-of-flight secondary ion mass spectrometer. Conductive atomic force microscopic measurements were performed on a Solver P47-PRO (NT-MDT Co., Moscow, Russia) microscope to monitor the local conducting behavior of the perovskite films.

The J-V curves of the 0.08-cm^2 $FA_{0.8}Cs_{0.2}Pb_{0.5}Sn_{0.5}I_3$ photodetectors were acquired by a Keithley 2400 source meter in the dark and under AM 1.5G white light illumination (100 mW/cm^2). LDR of the device was acquired under different input light intensities of the simulated standard solar irradiation attenuated using Thorlabs metallic-coated neutral density filters. These measurements were done in a glove box with N_2 atmosphere. The trap state density (tDOS) of the perovskite film was evaluated through space charge–limited current measurements in an ITO/PEDOT:PSS/perovskite/MoO_3/Au configuration. EQE profiles of the device were measured by the Enlitech EQE system (Enlitech QE-M110) with a silicon diode as a reference cell. Monochromatic light was generated from an Enlitech lamp source with a monochromator. Transient photovoltage (TPV) decay was measured through connecting the device to a digital storage oscilloscope (Keysight, 1 GHz Agilent DSO7104B) to form an open-circuit condition and illuminated by a standard solar simulator. An attenuated 337-nm laser pulse (with a frequency of 20 Hz and a pulse width of <2.5 ns) was applied as a small perturbation on the device. TPC measurement was performed similarly, by connecting the device and the oscilloscope to form a short-circuit condition. In both measurements, the impedance of the oscilloscope was set to 50 ohm. The tDOS, EQE, TPV, and TPC measurements were performed upon device encapsulation in an ambient environment. All the above measurements were performed by irradiating the perovskite devices from the ITO electrode. Furthermore, photoelectrical measurements of the 7.85×10^{-5} cm^2 perovskite photodetectors and 9×10^{-4} cm^2 1T-1PD retinomorphic sensors were performed in vacuum on a Keithley 4200 semiconductor parameter analyzer coupled probe station. Commercially available light emitting diode lamps with wavelengths of 460, 530, 640, 860, and 940 nm were used as the light sources for these devices and illuminated from the Au electrode side. The illuminating intensity, duration, and frequency of the incident light were controlled by a RXN3505 M DC power supply and a DORI RH-D12 single-chip microcontroller. The illumination intensity projected onto the devices was calibrated using a Li-250A Light Meter (LI-COR Inc.).

Supplementary Materials

The PDF file includes:
Supplementary Text
Figs. S1 to S30
Tables S1 to S3
Legends for movies S1 to S8
References

Other Supplementary Material for this manuscript includes the following:
Movies S1 to S8

REFERENCES AND NOTES

1. L. Gionfrida, D. Kim, D. Scaramuzza, D. Farina, R. D. Howe, Wearable robots for the real world need vision. *Sci. Robot.* **9**, eadj8812 (2024).
2. H. Xia, Y. Zhang, N. Rajabi, F. Taleb, Q. Yang, D. Kragic, Z. Li, Shaping high-performance wearable robots for human motor and sensory reconstruction and enhancement. *Nat. Commun.* **15**, 1760 (2024).
3. D. Kim, B. B. Kang, K. B. Kim, H. Choi, J. Ha, K. Cho, S. Jo, Eyes are faster than hands: A soft wearable robot learns user intention from the egocentric view. *Sci. Robot.* **4**, eaav2949 (2019).
4. G. Underwood, Reptilian retinas. *Nature* **167**, 183–185 (1951).
5. P. S. Gehring, *Leaf-tailed Geckos—The Complete Uroplatus* (Edition Chimaira, 2020).
6. R. Llinas, W. Precht, *Neurophysiology of the Anuran Visual System in Frog Neurobiology, A Handbook* (Springer, 1976).
7. K. Donner, C. A. M. Yovanovich, A frog's eye view: Foundational revelations and future promises. *Semin. Cell Dev. Biol.* **106**, 72–85 (2020).
8. T. Gollisch, M. Meister, Eye smarter than scientists believed: Neural computations in circuits of the retina. *Neuron* **65**, 150–164 (2010).
9. F. Zhou, Y. Chai, Near-sensor and in-sensor computing. *Nat. Electron.* **3**, 664–671 (2020).
10. J. Michel, J. Liu, L. C. Kimerling, High-performance Ge-on-Si photodetectors. *Nat. Photon.* **4**, 527–534 (2010).
11. P. Cheben, R. Halir, J. H. Schmid, H. A. Atwater, D. R. Smith, Subwavelength integrated photonics. *Nature* **560**, 565–572 (2018).
12. P. Martyniuk, P. Wang, A. Rogalski, Y. Gu, R. Jiang, F. Wang, W. Hu, Infrared avalanche photodiodes from bulk to 2D materials. *Light Sci. Appl.* **12**, 212 (2023).
13. S. Seo, S. Jo, S. Kim, J. Shim, S. Oh, J. Kim, K. Heo, J. Choi, C. Choi, S. Oh, D. Kuzum, H.-S. P. Wong, J. Park, Artificial optic-neural synapse for colored and color-mixed pattern recognition. *Nat. Commun.* **9**, 5106 (2018).
14. L. Mennel, J. Symonowicz, S. Wachter, D. K. Polyushkin, A. J. Molina-Mendoza, T. Mueller, Ultrafast machine vision with 2D material neural network image sensors. *Nature* **579**, 62–66 (2020).
15. C. Wang, S. Liang, S. Wang, P. Wang, Z. Li, Z. Wang, A. Gao, C. Pan, C. Liu, J. Liu, H. Yang, X. Liu, W. Song, C. Wang, B. Cheng, X. Wang, K. Chen, Z. Wang, K. Watanabe, T. Taniguchi, J. J. Yang, F. Miao, Gate-tunable van der Waals heterostructure for reconfigurable neural network vision sensor. *Sci. Adv.* **6**, eaba6173 (2020).
16. C. Choi, J. Leem, M. Kim, A. Taqieddin, C. Cho, K. W. Cho, G. J. Lee, H. Seung, H. J. Bae, Y. M. Song, T. Hyeon, N. R. Aluru, S. Nam, D. Kim, Curved neuromorphic image sensor array using a MoS_2-organic heterostructure inspired by the human visual recognition system. *Nat. Commun.* **11**, 5934 (2020).
17. L. Tong, Z. Peng, R. Lin, Z. Li, Y. Wang, X. Huang, K. Xue, H. Xu, F. Liu, H. Xia, P. Wang, M. Xu, W. Xiong, W. Hu, J. Xu, X. Zhang, L. Ye, X. Miao, 2D materials-based homogeneous transistor-memory architecture for neuromorphic hardware. *Science* **373**, 1353–1358 (2021).
18. L. Pi, P. Wang, S. Liang, P. Luo, H. Wang, D. Li, Z. Li, P. Chen, X. Zhou, F. Miao, T. Zhai, Broadband convolutional processing using band-alignment-tunable heterostructures. *Nat. Electron.* **5**, 248–254 (2022).
19. Z. Zhang, S. Wang, C. Liu, R. Xie, W. Hu, P. Zhou, All-in-one two-dimensional retinomorphic hardware device for motion detection and recognition. *Nat. Nanotechnol.* **17**, 27–32 (2022).
20. J. Meng, T. Wang, H. Zhu, L. Ji, W. Bao, P. Zhou, L. Chen, Q. Sun, D. W. Zhang, Integrated in-sensor computing optoelectronic device for environment-adaptable artificial retina perception application. *Nano Lett.* **22**, 81–89 (2022).
21. G. Zhang, Z. Zhang, X. Chen, L. Kang, Y. Li, F. Wang, L. Shi, K. Shi, Z. Liu, J. Tian, T. Lu, J. Zhang, Broadband sensory networks with locally stored responsivities for neuromorphic machine vision. *Sci. Adv.* **9**, eadi5104 (2023).
22. X. Fu, T. Li, B. Cai, J. Miao, G. N. Panin, X. Ma, J. Wang, X. Jiang, Q. Li, Y. Dong, C. Hao, J. Sun, H. Xu, Q. Zhao, M. Xia, B. Song, F. Chen, X. Chen, W. Lu, W. Hu, Graphene/$MoS_{2-x}O_x$/graphene photomemristor with tunable non-volatile responsivities for neuromorphic vision processing. *Light Sci. Appl.* **12**, 39 (2023).
23. G. Wu, X. Zhang, G. Feng, J. Wang, K. Zhou, J. Zeng, D. Dong, F. Zhu, C. Yang, X. Zhao, D. Gong, M. Zhang, B. Tian, C. Duan, Q. Liu, J. Wang, J. Chu, M. Liu, Ferroelectric-defined reconfigurable homojunctions for in-memory sensing and computing. *Nat. Mater.* **22**, 1499–1506 (2023).
24. X. Pan, J. Shi, P. Wang, S. Wang, C. Pan, W. Yu, B. Cheng, S. Liang, F. Miao, Parallel perception of visual motion using light-tunable memory matrix. *Sci. Adv.* **9**, eadi4083 (2023).
25. Y. Zhou, J. Fu, Z. Chen, F. Zhuge, Y. Wang, J. Yan, S. Ma, L. Xu, H. Yuan, M. Chan, X. Miao, Y. He, Y. Chai, Computational event-driven vision sensors for in-sensor spiking neural networks. *Nat. Electron.* **9**, 870–878 (2023).
26. P. Huang, B. Jiang, H. Chen, J. Xu, K. Wang, C. Zhu, X. Hu, D. Li, L. Zhen, F. Zhou, J. Qin, C. Xu, Neuro-inspired optical sensor array for high-accuracy static image recognition and dynamic trace extraction. *Nat. Commun.* **14**, 6736 (2023).
27. D. Xiang, T. Liu, J. Xu, J. Y. Tan, Z. Hu, B. Lei, Y. Zheng, J. Wu, A. H. C. Neto, L. Liu, W. Chen, Two-dimensional multibit optoelectronic memory with broadband spectrum distinction. *Nat. Commun.* **9**, 2966 (2018).
28. H. Jang, C. Liu, H. Hinton, M. Lee, H. Kim, M. Seol, H. Shin, S. Park, D. Ham, An atomically thin optoelectronic machine vision processor. *Adv. Mater.* **32**, 2002431 (2020).
29. J. Lee, S. Tan, S. I. Seok, Y. Yang, N. Park, Rethinking the A cation in halide perovskites. *Science* **375**, 6583 (2022).
30. Y. Zhou, L. M. Herz, A. K.-Y. Jen, M. Saliba, Advances and challenges in understanding the microscopic structure–property–performance relationship in perovskite solar cells. *Nat. Energy* **7**, 794–807 (2022).

31. H. Zhang, L. Pfeifer, S. M. Zakeeruddin, J. Chu, M. Gratzel, Tailoring passivators for highly efficient and stable perovskite solar cells. *Nat. Rev. Chem.* **7**, 632–652 (2023).

32. Q. Chen, Y. Zhang, S. Liu, T. Han, X. Chen, Y. Xu, Z. Meng, G. Zhang, X. Zheng, J. Zhao, G. Cao, G. Liu, Switchable perovskite photovoltaic sensors for bioinspired adaptive machine vision. *Adv. Intell. Syst.* **2**, 2000122 (2020).

33. P. Calado, A. M. Telford, D. Bryant, X. Li, J. Nelson, B. C. O'Regan, P. R. F. Barnes, Evidence for ion migration in hybrid perovskite solar cells with minimal hysteresis. *Nat. Commun.* **7**, 13831 (2016).

34. C. Eames, J. M. Frost, P. R. F. Barnes, B. C. O'Regan, A. Walsh, M. S. Islam, Ionic transport in hybrid lead iodide perovskite solar cells. *Nat. Commun.* **6**, 7497 (2015).

35. A. Senocrate, J. Maier, Solid-state ionics of hybrid halide perovskites. *J. Am. Chem. Soc.* **141**, 8382–8396 (2019).

36. Y. Yuan, Q. Wang, J. Huang, *Ion Migration in Hybrid Perovskite Solar Cells* (Springer, 2016).

37. W. Tress, N. Marinova, T. Moehl, S. M. Zakeeruddin, M. K. Nazeeruddina, M. Grätzela, Understanding the rate-dependent J-V hysteresis, slow time component, and aging in $CH_3NH_3PbI_3$ perovskite solar cells: The role of a compensated electric field. *Energ. Environ. Sci.* **8**, 995–1004 (2015).

38. Y. Zhang, M. Liu, G. E. Eperon, T. C. Leijtens, D. McMeekin, M. Saliba, W. Zhang, M. D. Bastiani, A. Petrozza, L. M. Herz, M. B. Johnston, H. Lin, H. J. Snaith, Charge selective contacts, mobile ions and anomalous hysteresis in organic–inorganic perovskite solar cells. *Mater. Horiz.* **2**, 315–322 (2015).

39. J. Zhou, H. Qiu, T. Wen, Z. He, C. Zou, Y. Shi, L. Zhu, C. Chen, G. Liu, S. Yang, F. Liu, Z. Yang, Acidity control of interface for improving stability of all-perovskite tandem solar cells. *Adv. Energy Mater.* **13**, 2300968 (2023).

40. A. Darmont, *High Dynamic Range Imaging: Sensors and Architectures* (SPIE, 2013).

41. P. Baldelli, N. Phelan, G. Egan, Investigation of the effect of anode/filter materials on the dose and image quality of a digital mammography system based on an amorphous selenium flat panel detector. *Br. J. Radiol.* **83**, 290–295 (2010).

42. E. Seeram, *Computed Tomography: Physical Principles, Clinical Applications, and Quality Control* (Elsevier Health Sciences, 2015).

43. C. H. Ye, D.-H. Lee, CMOS image sensor: Characterizing its PRNU (photo-response non-uniformity). *Proc. SPIE* **10757**, 41–47 (2018).

44. S. Kasap, P. Capper, *Springer Handbook of Electronic and Photonic Materials* (Springer, 2017), chapter 45.

45. Z. Song, X. Du, X. He, H. Wang, Z. Liu, H. Wu, H. Luo, L. Jin, L. Xu, Z. Zheng, G. Niu, J. Tang, Rheological engineering of perovskite suspension toward high-resolution X-ray flat-panel detector. *Nat. Commun.* **14**, 6865 (2023).

46. R. Lin, Y. Wang, Q. Lu, B. Tang, J. Li, H. Gao, Y. Gao, H. Li, C. Ding, J. Wen, P. Wu, C. Liu, S. Zhao, K. Xiao, Z. Liu, C. Ma, Y. Deng, L. Li, F. Fan, H. Tan, All-perovskite tandem solar cells with 3D/3D bilayer perovskite heterojunction. *Nature* **620**, 994–1000 (2023).

47. A. M. Najarian, M. Vafaie, A. Johnston, T. Zhu, M. Wei, M. I. Saidaminov, Y. Hou, S. Hoogland, F. P. G. Arquer, E. H. Sargent, Sub-millimetre light detection and ranging using perovskites. *Nat. Electron.* **5**, 511–518 (2022).

48. J. Ohta, *Smart CMOS Image Sensors and Applications* (CRC Press, 2017).

49. X. Gong, M. Tong, Y. Xia, W. Cai, J. S. Moon, Y. Cao, G. Yu, C. Shiei, B. Nilsson, A. J. Heeger, High-detectivity polymer photodetectors with spectral response from 300 nm to 1450 nm. *Science* **325**, 1665–1667 (2009).

50. R. Chang, Q. Chen, W. Shen, Y. Zhang, B. Zhang, S. Wang, Controllable switching between highly rectifying schottky and p-n junctions in an ionic MoS_2 device *Adv. Funct. Mater.* **33**, 2301010 (2023).

51. S. Chen, Y. Fu, M. Ishaq, C. Li, D. Ren, Z. Su, X. Qiao, P. Fan, G. Liang, J. Tang, Carrier recombination suppression and transport enhancement enable high-performance self-powered broadband Sb_2Se_3 photodetectors. *InfoMat.* **5**, e12400 (2023).

52. Y. Lu, T. Chen, N. Mkhize, R. Chang, Y. Sheng, P. Holdway, H. Bhaskaran, J. H. Warner, $GaS:WS_2$ heterojunctions for ultrathin two-dimensional photodetectors with large linear dynamic range across broad wavelengths. *ACS Nano* **15**, 19570–19580 (2021).

53. D. Luo, R. Su, W. Zhang, Q. Gong, R. Zhu, Minimizing non-radiative recombination losses in perovskite solar cells. *Nat. Rev. Mater.* **5**, 44–60 (2020).

54. Y. Li, Z. Chen, B. Yu, S. Tan, Y. Cui, H. Wu, Y. Luo, J. Shi, D. Li, Q. Meng, Efficient, stable formamidinium-cesium perovskite solar cells and minimodules enabled by crystallization regulation. *Joule* **6**, 676–689 (2022).

55. Z. Yang, Z. Yu, H. Wei, X. Xiao, Z. Ni, B. Chen, Y. Deng, S. N. Habisreutinger, X. Chen, K. Wang, J. Zhao, P. N. Rudd, J. J. Berry, M. C. Beard, J. Huang, Enhancing electron diffusion length in narrow-bandgap perovskites for efficient monolithic perovskite tandem solar cells. *Nat. Commun.* **10**, 4498 (2019).

56. Z. Yu, J. Wang, B. Chen, M. A. Uddin, Z. Ni, G. Yang, J. Huang, Solution processed ternary tin (II) alloy as hole-transport layer of Sn-Pb perovskite solar cells for enhanced efficiency and stability. *Adv. Mater.* **34**, 676–689 (2022).

57. J. Cao, H. Loi, Y. Xu, X. Guo, N. Wang, C. Liu, T. Wang, H. Cheng, Y. Zhu, M. G. Li, W. Wong, F. Yan, High-performance tin-lead mixed-perovskite solar cells with vertical compositional gradient. *Adv. Mater.* **34**, e2107729 (2022).

58. Y. Zhang, S. He, W. Guo, Y. Hu, J. Huang, J. R. Mulcahy, W. D. Wei, Surface-plasmon-driven hot electron photochemistry. *Chem. Rev.* **118**, 2927–2954 (2018).

59. Z. Ni, H. Jiao, C. Fei, H. Gu, S. Xu, Z. Yu, G. Yang, Y. Deng, Q. Jiang, Y. Liu, J. Huang, Evolution of defects during the degradation of metal halide perovskite solar cells under reverse bias and illumination. *Nat. Energy* **7**, 65–73 (2022).

60. Y. Lin, B. Chen, Y. Fang, J. Zhao, C. Bao, Z. Yu, Y. Deng, P. N. Rudd, Y. Yan, Y. Yuan, J. Huang, Excess charge-carrier induced instability of hybrid perovskites. *Nat. Commun.* **9**, 4981 (2018).